Surveys in Geophysics
https://doi.org/10.1007/s10712-018-9493-z

Improvement of Ground Penetrating Radar (GPR) Data Interpretability by an Enhanced Inverse Scattering Strategy

Raffaele Persico[1,2] · Giovanni Ludeno[3] · Francesco Soldovieri[3] · Albéric De Coster[4] · Sébastien Lambot[4]

Received: 30 May 2018 / Accepted: 23 July 2018

Abstract

This paper is inserted into the framework of inverse scattering with application to Ground Penetrating Radar (GPR) data and is meant to provide a method helping to apply inverse scattering algorithms to electrically large investigation domains. In particular, we focus on the depth slices that are particularly important in application on cultural heritage and propose in relationship with the depth slices a strategy that we will call "shifting zoom" that is specifically a method to mitigate the effects of the limited view angle in the linear tomographic inversion applied to GPR data. In particular, this paper is an extended version of the contribution (Persico et al. in: Proceedings of Imeko international conference on metrology for archaeology and cultural heritage, Lecce, Italy, 2017a), published in the Proceedings of the conference metrology for archaeology 2017. We propose here a validation of the shifting zoom versus experimental data gathered in a controlled test site, and we will show the effect of the shifting zoom on depth slices achieved from these data after a linear inverse scattering processing has been applied for their focusing.

Keywords GPR · Depth slices · Shifting zoom

✉ Raffaele Persico
r.persico@ibam.cnr.it

Giovanni Ludeno
ludeno.g@irea.cnr.it

Francesco Soldovieri
soldovieri.f@irea.cnr.it

Albéric De Coster
alberic.decoster@uclouvain.be

Sébastien Lambot
sebastien.lambot@uclouvain.be

1 Institute for the Archaeological and Monumental Heritage IBAM-CNR, Via Monteroni, Campus Universitario, 73100 Lecce, Italy

2 International Telematic University Uninettuno UTIU, Corso Vittorio Emanuele II n. 39, 00186 Rome, Italy

3 Institute for the electromagneting sensing of the environment IREA-CNR, Via Diocleziano n. 328, 80124 Naples, Italy

4 Universitè catholique de Louvain, Croix du Sud 2/L7.05.02, 1348 Louvain-la-Neuve, Belgium

Published online: 09 August 2018

1 Introduction

Microwave imaging algorithms are of interest in several fields and in particular also with regard to GPR data. The most spread kinds of linear algorithm for the focusing of GPR data are undoubtedly migration algorithms, also because they are implemented as subroutines within common commercial codes (as, e.g., Reflexw and GPRSlice) that also allow many further preprocessing steps needed in practical circumstances, such as a suitable zero timing, 1D and 2D filtering algorithms, construction of depth slices, evaluation of the propagation velocity by means of the diffraction hyperbolas and so on.

Migration algorithms, historically imported from the seismics, are based on the Born approximation and contain further approximation beyond the linearization. In particular, they are based on the hypothesis of lossless medium and on the hypothesis of targets buried at a level deeper than the central wavelength in the soil (Persico 2014). Migration algorithms are essentially inversion approaches where the inverse operator is approximated with the adjoint operator (Bertero and Boccacci 1998).

This constitutes a meaningful limitation, and several efforts have been done in order to propose a more refined model for the inversion. In particular, linear algorithms still based on the Born approximation have been proposed, but relying on a numerical formulation based on the expansion of the object function along a pre-chosen functional basis. This involves the possibility to remove some limits, but increases the computational burden, due to the construction of a matrix to be inverted. As a matter of fact, this compels us to consider an investigation domain whose length is of the order of ten wavelengths at most (Caorsi and Pastorino 2000), and the average size of the domain is of course even smaller in 3D inversions (Gennarelli et al. 2015), whereas the length of the observation line in practical cases can be of the order of hundreds or even thousands of wavelengths. This computational problem does not change too much if other linear approximations different from the Born model are adopted (Liseno et al. 2004), and can become even worse if a nonlinear approach is adopted (in which case also the problem of the local minima has to be considered). The computational problem is not only with regard to the calculation of the matrix but also with regard to the calculation of its singular value decomposition (SVD), indispensable in order to perform a regularized inversion, stable versus noise, model error and uncertainties. In fact, the calculation of the SVD requires a sufficient amount of RAM memory, which means that beyond a certain size of the investigation domain depending on the available calculation hardware, it is impossible to perform the inversion.

So, the adaptation of a linear inversion algorithm to a large-scale problem requires some trick. The most immediate gimmick in this sense is to divide the observation line into several adjacent sub-segments, each of which short enough to allow a linear inversion relative to an investigation domain underlying it. Then, the achieved sub-reconstructions are joined side by side (Pettinelli et al. 2009).

In Persico and Sala (2014), a first version of the shifting zoom proposed here was presented, and the strategy was perfected in the paper Persico et al. (2017b). Here, we extend the contribution proposed at the Metroarcheo conference (Persico et al. 2017a) proposing the effect of the shifting zoom on depth slices relative to data gathered in a test site. With respect to Persico and Sala (2014), the central belt (see next section) is here better defined, whereas in that paper it was equal to one half of the investigation domain, which generated visible spurious "seams" between any adjacent reconstruction. With respect to Persico et al. (2017b), here the effect of the shifting zoom on the depth slices is shown, whereas only vertical B-scans had been considered up to that moment.

This is an important aspect, because depth slices are able to provide a map image of the prospected structures, which is essential in application on cultural heritage. For this reason, a session specifically devoted to the depth slices is provided in the following. With respect to the paper (Persico et al. 2017a), instead, here we show the effect of the shifting zoom when the target crosses the boundaries of their investigation domain. We will show in particular that the initial abscissa of the data can be important when adjacent domains are adopted, whereas the result is better and less influenced by this parameter when a shifting zoom is performed.

The work is organized as follows: In the next section, the relevance of the depth slices is outlined. Then, the formulation of the problem is provided. In Sect. 4, the shifting zoom is explained. In Sect. 5, experimental results are proposed and discussed. Conclusions follow.

2 Depth Slices

Depth slices are a technique to retrieve pseudo-horizontal slices at progressive depth level in the soil or in a wall. In cultural heritage applications, these images are often more important than those provided by the processed B-scans (Goodman et al. 1995; Conyers 2004), because they can provide information about the shape and size of ancient building (Linford and Linford 2004; Piro et al. 2003), the path of ancient roads and more in general the ancient landscape (Campana and Piro 2009), the position of graves under the soil or under historical monuments (Bevan 1991; Utsi 2009; Trinks et al. 2010). The use of depth slices is common also beyond the field of the cultural heritage (Daniels 2004; Allred and Redman 2010) and is a representation shared also with other geophysical techniques. In particular, it is possible to retrieve GPR slices from seismic data or from geoelectrical data too (Leucci and Greco 2012), whereas magnetic data provide a slice as their normal kind of output, as is well known (Chianese et al. 2004).

Depth slices are customarily achieved representing all the echoes received at the same time depth, after processing the data. This means that the images are pseudo-horizontal, because the propagation velocity of the electromagnetic wave in the investigated medium is not homogeneous. In other words, in order to have a spatially horizontal slice, we should retrieve a suitably curved sheet-like slice in time domain. This is virtually never done because it is complicated and above all it is not easy to achieve a sufficiently precise evaluation of the propagation velocity of the wave as a function of the point. At any rate, in order to amortize this effect, it is customary to average a range of depth levels and take indeed the result of the process as depth slice. In this way, we not only average the discrepancies of the time–depth conversion from point to pint, but also mitigate the effect that some feature expected and described as "horizontal" of course are not perfectly horizontal, for example because of the different preservation states (in case of archaeological remains) of the buried structure from point to point. Consequently, a perfectly horizontal cut of the buried scenario in most cases would not provide a fully significant representation of the buried scenario. The amount of the averaged depth ranges is a compromise between the contrasting exigencies of including all the parts of a sub-horizontal structure (as, e.g., a buried floor) but not including different targets. There is no mathematical rule establishing the extension of the depth range, but an heuristically reasonable value should be related to the central wavelength of the electromagnetic radiation, to the depth of the targets looked for and to the vertical size of the targets of interest. On average, a value of a few nanoseconds, corresponding in general to a spatial range of the order of 15 or 20 cm, is a reasonable choice for prospecting on the soil, usually performed with antennas with central frequency from 200 to 600 MHz, at least for cultural heritage applications (Conyers and Goodman 1998). It is more well advised to restrict this range to the order of 1 ns (a very few cm) in cases of slices related to intra-wall prospecting or similar targets as, e.g., statues (Kadioglu and Kadioglu 2010).

Depth slices can also be easily and nicely inserted in a satellite map of the site (Trinks et al. 2014), which can be useful also in order to implement a virtual reconstruction (Gabellone et al. 2010). Finally, depth slices can be somehow interpolated in order to achieve a perspective reconstruction of the buried scenario. This is appealing in some cases but is a delicate operation because it involves the application of a threshold on the slices, or more in general on the data. In particular, very good images are achieved if a homogeneous target is embedded in a homogeneous scenario in a limited range of depth, as, for example, in Hansen and Johansen (2000); otherwise, the image can depend meaningfully on the threshold, which intrinsically introduces a degree of arbitrariness on the procedure. For this reason, here we will concentrate on the depth slices and in particular will propose a technique, the shifting zoom, that can improve them if a linear inversion algorithm (or also possibly a nonlinear inversion algorithm, not exploited in the present paper) is exploited within the data processing.

3 Formulation of the Problem

In electromagnetism, and in particular in GPR prospecting, the direct scattering problem is the relationship that relates the scattered field E_s generated by the buried targets and the unknown dielectric contrast χ.

The scattered field is the difference between the total field E_{tot} (i.e., the field physically present in the observation point) and the incident field E_{inc} (i.e., the field that we would record in the observation point in the absence of any buried target). The contrast is the difference between the (possibly complex) dielectric permittivity of the buried anomalies ε_s and that of the surrounding soil ε_r, normalized by the same permittivity of the soil.

In formulas

$$E_s(\mathbf{r}_o, \omega) = E_{tot}(\mathbf{r}_o, \omega) - E_{inc}(\mathbf{r}_o, \omega), \tag{1}$$

$$\chi(\mathbf{r}, \omega) = \frac{\varepsilon_r(\mathbf{r}, \omega) - \varepsilon_s(\mathbf{r}, \omega)}{\varepsilon_r(\mathbf{r}, \omega)}, \tag{2}$$

a multi-monostatic measurement configuration is meant, and, in particular, the incident field is modeled as the field generated by a unitary filamentary current placed at $\mathbf{r}_o$. The subscript "O" denotes the observation point, belonging to the observation domain. Theoretically, the total field is the measured datum and the incident field in the observation point is calculated, but this is impractical due to the parametric uncertainties related to the problem at hand. Therefore, a quantity resembling the scattered field is retrieved in approximate ways as interface muting or background removal (Persico et al. 2016). Λ is the investigation domain, i.e., the spatial region where the targets are assumed to reside, and $\mathbf{r}$ is the point within the investigation domain.

Under the Born approximation, the scattering problem can be formulated as:

$$E_s(\mathbf{r}_o, \omega) = k_b^2 \iint_{\Lambda} G(\mathbf{r}_o - \mathbf{r}', \omega) E_{inc}(\mathbf{r}_o, \mathbf{r}', \omega) \chi(\mathbf{r}') d\mathbf{r}', \tag{3}$$

where G is the Green's function and k_b is the wave number in the reference medium. Here, we will make use of a homogeneous reference scenario, which makes both incident field and Green's function proportional to a Hankel function $H_0^{(2)}(\cdot)$ (Persico et al. 2016) of second kind and zero order. Consequently, Eq. (3) is particularized into:

$$E_s(\mathbf{r}_o,\omega) = j\frac{\omega\mu_0}{8}k_b^2 \iint\limits_{\Lambda} \left[H_0^{(2)}\left(k_b\left|\mathbf{r}_o - \mathbf{r}'\right|\right)\right]^2 \chi(\mathbf{r}')\mathrm{d}\mathbf{r}' \tag{4}$$

The right-hand side of Eq. (4) quantifies the linear operator $\boldsymbol{L}$ relating the unknown contrast function to the scattered field data. This linear integral operator $\boldsymbol{L}$ can be expressed through its singular value decomposition (SVD) (Bertero and Boccacci 1998). Then, the contrast can be retrieved as

$$\boldsymbol{\chi}(\mathbf{r}) = \sum_{n=1}^{\infty} \frac{1}{\sigma_n}\langle \mathbf{E}_s, \mathbf{u}_n\rangle \mathbf{v}_n(\mathbf{r}) \quad \mathbf{r} \in \Lambda, \tag{5}$$

where σ_n is the nth singular value, $\boldsymbol{v}_n$ and $\boldsymbol{u}_n$ are the nth left-hand-side and right-hand-side singular function, respectively.

However, the ill-posedness reverses on the fact that the singular values vanish versus the index, which reverses into an instability of the solution as is well known. We will adopt here one of the classical regularization schemes, namely the truncated SVD (TSVD), where the solution is provided by:

$$\hat{\boldsymbol{\chi}}(\mathbf{r}) = \sum_{n=1}^{T} \frac{1}{\sigma_n}\langle \mathbf{E}_s, \mathbf{u}_n\rangle \mathbf{v}_n(\mathbf{r}) \quad \mathbf{r} \in \Lambda \tag{6}$$

T is an integer number usually provided by a threshold applied on the singular values, and its choice is a compromise between the accuracy and the robustness of the solution. In practical cases, it is in general well advised to try different thresholds and choose heuristically the one that provides the apparently best solution. We also have followed this way, so it is to be taken for granted that the results that will be shown have been achieved with the heuristically best threshold.

4 The Shifting Zoom

In this section, we will show specifically what we mean with "shifting zoom." As said, a long investigation domain in general cannot be "inverted" making use of a unique global discretized operator. Consequently, in order to invert a long investigation domain, the most natural choice is to adopt subsequent adjacent investigation domains along the radar profile and consequently to adopt subsequent observation lines superposed adjacent to each other and superposed to the relative own investigation domains, as shown in Fig. 1.

When performing adjacent inversions, some care has to be taken for the correct hanging of the subsequent "pieces of reconstruction." In particular, the last measurement point exploited for the nth inversion should be re-exploited as the first measurement point exploited for the $(n+1)$th inversion; otherwise, a shift arises and accumulates progressively between the nth observation and the nth investigation domain.

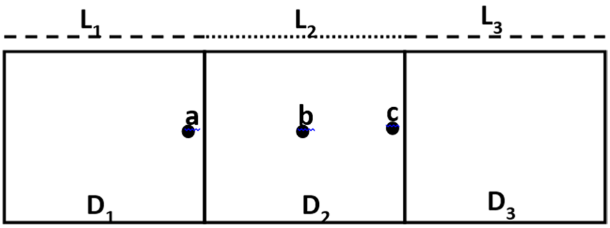

Fig. 1 Pictorial scheme for an inversion of a long radar image making use of adjacent investigation–observation domains

Indeed, it is not a mathematical rule that each observation line is exactly superposed to its relative investigation domain. In particular, the observation line might be longer than the investigation domain in order to enhance the maximum view angle (Persico 2014) under which the targets within that relative investigation domain are seen. The drawback is that the scattering model of Eq. (3) takes for granted that the possible targets are placed only within the investigation domain, so that in a practical case any target present outside it is a potential source of errors and artefacts, which is not acceptable. So, the choice of Fig. 1 is the most reasonable from a practical point of view.

Unavoidably, however, this choice introduces a problem of limited view angle for the targets peripheral with respect to the "current" investigation domain where they are placed. In particular, looking at Fig. 1, target ***c*** is peripheral with respect to the observation line L_2. Moreover, target ***a*** might cause artefacts in the investigation domain D_2, because it is quite probably perceived by the antennas when they pass on the left edge of L_2. Clearly, the problem of the peripheral targets (that are seen under a reduced and asymmetric comprehensive maximum view angle) and the problem of the external targets close to the investigation domain that are possible sources of artefacts within the current investigation domains are two sides of the same coin. In particular, from Fig. 1, clearly target ***a*** is also peripheral with respect to D_1 and target ***c*** is also a possible source of artefacts in D_3. However, neither ***a*** nor ***c*** is target peripheral with respect to the comprehensively gathered profile, and no one of them is an external target with respect to the comprehensive observation line: The problem arises by the subdivision of the radar profile into adjacent investigation–observation domains. Of course, there is also the possibility that a target crosses the edge between two adjacent domains. Such a case is enclosed in the considered records, because it can be seen as a couple of adjacent targets, one of which is placed on the left-hand side and one on the right-hand side of the edge.

The shifting zoom consists of making use of suitably overlapped investigation–observation domains instead of adjacent ones, as described in Fig. 2. The method consists in retaining only the central belt of the reconstruction achieved for the current investigation domain. In particular, the reconstruction achieved within the nth investigation domain is a matrix $A(i, j)$ of $n \times m$ pixels, and its central belt can be defined as the

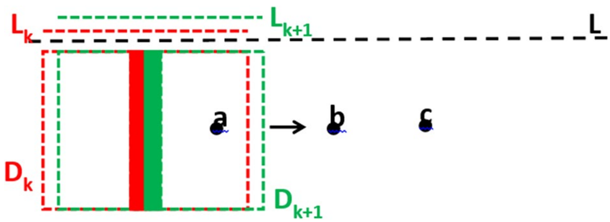

Fig. 2 Pictorial scheme of the shifting zoom

column $A(i, (m+1)/2)$ $(i=1\ldots n)$ if m is odd, or the two central columns $A(i, (m/2))$ and $A(i, (m/2)+1)$ $(i=1\ldots n)$ if m is even.

After retaining this central belt, the subsequent investigation domain is shifted of the amount of this belt with respect to the previous one. In particular, in Fig. 2 the generic kth investigation domain is indicated in red, and its central belt is colored in red too. The homologous areas with respect to the $(k+1)$th investigation domain are instead labeled in green. Also the observation lines have to be coherently shifted, so to keep them hanging to the relative underlying investigation domains, as shown in Fig. 2. This compels us to adopt a size of the pixel and a spatial step of the data equal to each other or at least chosen with an integer ratio between them.

When we exploit a shifting zoom, the joined reconstructions are relative only to the central belts of the subsequent investigation–observation domains, and therefore no peripheral target is artificially created nor do we have targets external to the current investigation domains that affect meaningfully the reconstruction. In fact, the external targets carry out an influence above all on the external part of the current investigation domain closer to them. The schematic proposed does not include the left side half of the first investigation domain (before the "first central belt") and the right side half of the last investigation domain (after the "last central belt"). However, these two halves of the first and of the last investigation domain can trivially be joined to the reconstruction, so as to achieve a reconstruction relative to the entire observation line, where only the really peripheral targets are peripheral and where only the really external targets close to the observation line can provide some artefacts. These drawbacks are physically unavoidable, and it is never a good choice to cut the reconstruction in order to avoid them. The computational price to be paid for the application of the shifting zoom is that the number of investigation–observation domains to be considered is higher than that needed when exploiting adjacent investigation–observation domains. In particular, the number of inversions that we have to perform along the entire observation line is of the order of m times those that we would have to do with adjacent domains, where m is as said the number of columns of the matrix $A(i, j)$ representing any sub-reconstruction. However, this does not mean that we have a computational burden m times larger or that we need a RAM memory m times larger. In fact, the matrix of the system is the same at all times, so that its elements can be calculated once and for all, and its SVD can be performed once and for all. The only thing that really needs to be repeated many more times is essentially a matrix–vector product, which is a fast and computationally not a demanding operation.

5 Experimental Results

The first results that we are going to show have been gathered with a GPR system implemented with a vector network analyzer (VNA), which constituted a stepped-frequency continuous-wave (SFCW) radar system (ZVRE, Rohde & Schwarz, Munich, Germany) and a linearly polarized, double-ridged broadband horn antenna (BBHA 9120 A, Schwarzbeck Mess-Elektronik, Schönau, Germany) exploited simultaneously as transmitter and receiver. So, the system is rigorously monostatic. The antenna nominal frequency band ranges from 0.8 to 5.0 GHz, and its isotropic gain ranges from 6 to 18 dBi. The relatively high directivity of the antenna (45°−3 dB beam width in the E-plane and 30° in the H-plane at 1 GHz) makes it immune to interference from external sources or reflectors, which enforces the homogeneous space reference model. The antenna was connected to the reflection port of the VNA via a high-quality *N*-type 50-Ohm coaxial cable.

The calibration of the VNA at the connection between the antenna feed point and the cable was achieved using an open-short-match calibration kit. After that, data were gathered at 1601 frequencies equally spaced ($\Delta f = 2$ MHz) between 800 and 4000 MHz.

The radar measurements were performed over a 3×3 m dry sand box with the antenna aperture at height 1 cm above the sand. A copper sheet assumed as a perfect electrical conductor (PEC) was installed at the bottom of the 0.86-m-thick sand layer to control the boundary conditions in the model. The targets were three PVC pipes of 1.20 m length and 50 mm diameter with a thickness of 1.8 mm and were buried at 0.07, 0.29 and 0.51 m depth, respectively. The three pipes were displaced about parallel to each other, and their horizontal distance from the start point of the B-scans was about equal to 0.47, 1.17 and 1.97 m, respectively. The pipes were filled with air. The radar system was installed on a *XYZ* automated positioning table to automatically acquire the data over a 2.40-m-long profile with a position step of 1 cm. The radar profiles were transversal with respect to the pipes.

Following the near-field radar antenna model described in Lambot and André (2014), the antenna global reflection and transmission functions were determined. Then, in order to remove a part of the antenna effects, the free-space response of the antenna was subtracted from the scattering coefficient $S_{11}(f)$ (Collin 2001). The frequency-domain radar data were subsequently converted into the time domain using the inverse Fourier transform, and a zero timing together with a background removal was subsequently applied to highlight the targets.

We have gathered comprehensively 49 B-scans, each of which 2.40 m long, with interline space of 5 cm. The measurement step was 1 cm along each B-scan. Then, we have inverted the data making use of three adjacent investigation–observation domains, each of which 80 cm long. The adopted data shift and subdivision make peripheral all the involved pipes. For the inversion, a relative permittivity equal to 2.37 [on the basis of the diffraction hyperbolas (Mertens et al. 2016)] has been adopted, and the TSVD has been regularized stopping the summation of Eq. (4) up to the last singular value higher or equal to -30 dB with respect to the first one. Three depth slices (at the depth levels of the pipes) achieved making use of three adjacent investigation–observation domains, each of which 80 cm large, are shown in Fig. 3. The images were achieved joining the homologous slices achieved with a shifting zoom. Three depth slices achieved with the

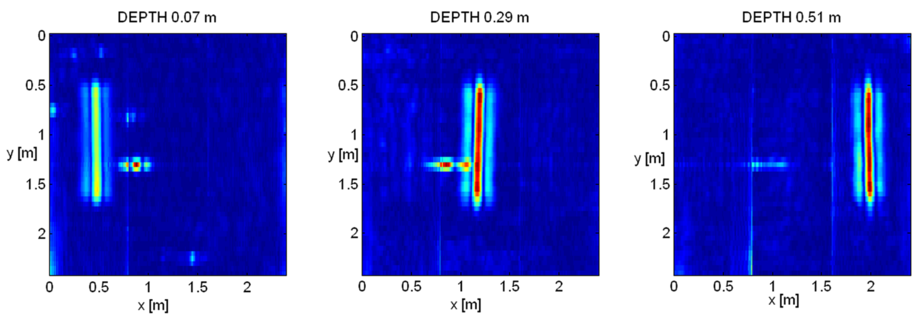

Fig. 3 Three slices at the depth levels of the three buried pipes. Inversions performed with three adjacent domains

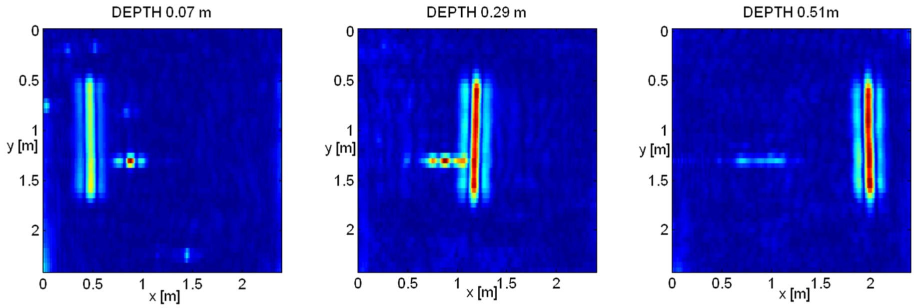

Fig. 4 Three slices at the depth levels of the three buried pipes. Inversions performed with shifting zoom

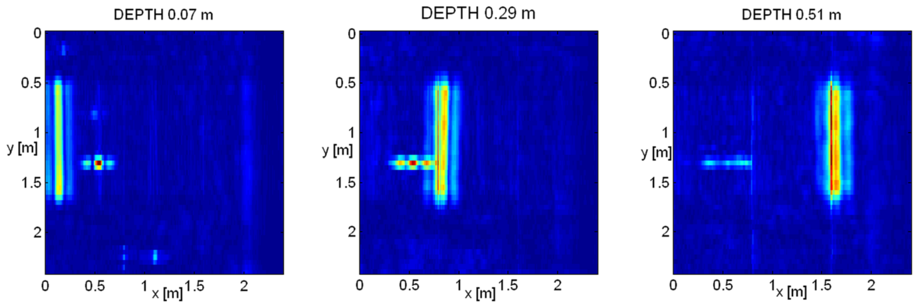

Fig. 5 Analogue of Fig. 3 with the comprehensive B-scan starting 0.35 m after the previous zero abscissa

shifting zoom at the same depth levels are shown in Fig. 4. As can be seen, in Fig. 4 we do not have seam effects that we see in Fig. 3, and that are related to the junction points between any two adjacent investigation domains. In particular, the seam effects in Fig. 3 are due to the fact that there is some difference between the average values of the reconstructed image in each adjacent investigation domain.

In Fig. 5, the homologue of Fig. 3 is achieved after a shift of the target of 0.35 m in the negative verse of the *x*-axis. Such a shift indeed has been simulated erasing the first data gathered in the first 0.35 m and prolonging on the other side the data with a zero padding again 0.35 m long. In other words, some true data on the left-hand side were replaced with the same number of null data on the right-hand side of the comprehensive observation line. Given the fact that the inversion domains were chosen 80 cm long, this is substantially equivalent to moving the targets 0.35 m back along the abscissa, so that now they are not any longer targets centered with respect to the investigation domain wherein they are inserted. The effect of this equivalent shift of the targets is clear in Fig. 5, where the second and the third pipes are still well recognizable but appear blurred due to their closeness or superposition to the edge between two adjacent investigation domains. In Fig. 6, the same data are inverted in the same way but for a shifting zoom for the joining of the subsequent inversion results. As can be seen, the bad effect of the edges has completely disappeared and the quality of the reconstruction is fully comparable with that of Fig. 4.

There are some extra anomalies beyond the three pipes visible in the reconstructions, which are probably due to some impurities in the test tank.

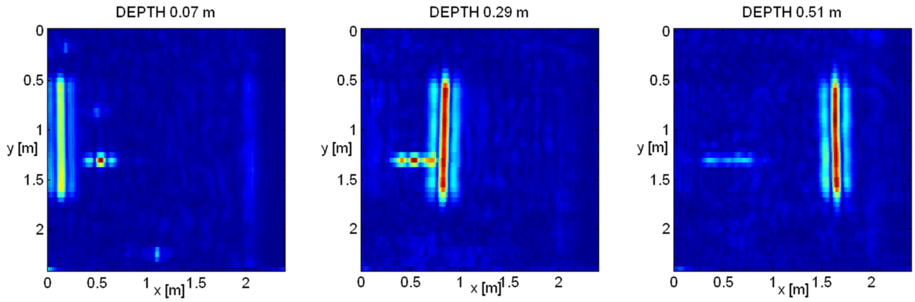

Fig. 6 Analogue of Fig. 4 with the comprehensive B-scan starting 0.35 m after the previous zero abscissa

6 Conclusions

In the present contribution, a shifting zoom procedure has been proposed for the numerical linear inversion of possibly electrically large investigation domains in the framework of GPR prospecting. We have shown experimental data gathered in a controlled situation and have shown in particular the effect of a shifting zoom on depth slices highlighting the presence of three pipes. Emphasis has been given to the depth slices because they are an instrument particularly relevant in the framework of the prospecting of archaeological sites or historical monuments. In particular, depth slices based on experimental data have been proposed here, achieved with a homemade MATLAB routine.

In the future, the procedure will be tested on data gathered in the field in an archaeological site or in a monument, probably an ancient church.

References

Allred BJ, Redman D (2010) Location of agricultural drainage pipes and assessment of agricultural drainage pipe conditions using ground penetrating radar. J Environ Eng Geophys 15:119–134

Bertero M, Boccacci P (1998) Introduction to inverse problems in imaging. Institute of Physics Publishing, Bristol

Bevan B (1991) The search for graves. Geophysics 56:1310–1319

Campana S, Piro S (2009) Seeing the unseen: geophysics and landscape archaeology. CRC Press, Boca Raton

Caorsi S, Pastorino M (2000) Two-dimensional microwave imaging approach based on a genetic algorithm. IEEE Trans Antennas Propag 48(3):370–372

Chianese D, D'Emilio M, Di Salvia S, Lapenna V, Ragosta M, Rizzo E (2004) Magnetic mapping, ground penetrating radar surveys and magnetic susceptibility. Measurements for the study of archaeological site of Serra di Vaglio (southern Italy). J Archaeol Sci 31:633–643

Collin RE (2001) Foundations of microwave engineering, 2nd edn. Wiley, Hoboken

Conyers LB (2004) Ground penetrating radar for archaeology. Alta Mira Press, Walnut Creek

Conyers LB, Goodman D (1998) Ground penetrating radar: an introduction for archaeologists. AltaMira Press, Walnut Creek

Daniels DJ (2004) Ground penetrating radar. IEEE, London

Gabellone F, Ferrario I, Giuri F, Limoncelli M (2010) Virtual Hierapolis: tra tecnicismo e realismo, in Arqueológica 2.0, II Congreso Internacional de Arqueología e Informática Gráfica, Patrimonio e Innovación, Sevilla, 16–19 Junio 2010, pp 279–284

Gennarelli G, Catapano I, Soldovieri F, Persico R (2015) On the achievable imaging performance in full 3-D linear inverse scattering. IEEE Trans Antennas Propag 63(3):1150–1155

Goodman D, Nishimura Y, Rogers JD (1995) GPR time slices in archaeological prospection. Archaeol Prospect 2:85–89

Hansen TB, Johansen PM (2000) Inversion scheme for ground penetrating radar that takes into account the planar air–soil interface. IEEE Trans Geosci Remote Sens 38(1):23–34

Kadioglu S, Kadioglu YK (2010) Picturing internal fractures of historical statues using ground penetrating radar method. Adv Geosci 24:23–34

Lambot S, André F (2014) Full-wave modeling of near-field radar data for planar layered media reconstruction. IEEE Trans Geosci Remote Sens 52:2295–2303

Leucci G, Greco F (2012) 3d electrical resistivity tomography to reconstruct archaeological features in the subsoil of the "spirito santo" church ruins at the site of occhiola' (sicily, italy). Archaeology 1(1):1–6

Linford NT, Linford PK (2004) Short report, ground penetrating radar survey over a Roman Building at Groudwell Ridge, Blunsdon St Andrew, Swindon, UK. Archaeol Prospect 11:49–55

Liseno A, Tartaglione F, Soldovieri F (2004) Shape reconstruction of 2d buried objects under a Kirchhoff approximation. IEEE Geosci Remote Sens Lett 1(2):118–121

Mertens L, Persico R, Matera L, Lambot S (2016) Smart automated detection of reflection hyperbolas in complex GPR images with no a priori knowledge on the medium. IEEE Trans Geosci Remote Sens 54(1):580–596

Persico R (2014) Introduction to ground penetrating radar: inverse scattering and data processing. Wiley, Hoboken. ISBN 9781118305003

Persico R, Sala J (2014) The problem of the investigation domain subdivision in 2D linear inversions for large scale GPR data. IEEE Geosci Remote Sens Lett 11(7):1215–1219. https://doi.org/10.1109/LGRS.2013.2290008

Persico R, Pochanin G, Ruban V, Orlenko A, Catapano I, Soldovieri F (2016) Performances of a microwave tomographic algorithm for GPR systems working in differential configuration. IEEE J Sel Topics Appl Earth Observ Remote Sens 9:1343–1356

Persico R, Ludeno G, Soldovieri F, De Coster A, Lambot S (2017a) Shifting zoom on a linear inverse scattering algorithm applied to GPR data. In: Proceedings of Imeko international conference on metrology for archaeology and cultural heritage, Lecce, Italy

Persico R, Ludeno G, Soldovieri F, De Coster A, Lambot S (2017b) 2D linear inversion of GPR data with a shifting zoom along the observation line. Remote Sensing 9:980. https://doi.org/10.3390/rs9100980

Pettinelli E, Di Matteo A, Mattei E, Crocco L, Soldovieri F, Redman DJ, Annan AP (2009) GPR response from buried pipes: measurement on field site and tomographic reconstructions. IEEE Trans Geosci Remote Sens 47(8):2639–2645

Piro S, Goodman D, Nishimura Y (2003) The study and characterization of Emperor Traiano's villa using high-resolution integrated geophysical surveys. Archaeol Prospect 10:1–25

Trinks I, Gansum T, Hinterleitner A (2010) Mapping iron-age graves in Norway using magnetic and GPR prospection. Antiquity 84:326

Trinks I, Neubauer W, Hinterleitner A (2014) First high-resolution GPR and magnetic archaeological prospection at the viking age settlement of Birka in Sweden. Archaeol Prospect 21:185–199

Utsi E (2009) The shrine of Edward the confessor: a study in multi-frequency GPR investigation. In: IEEE, 978-1-4244-4605-6/09